Seismic Anisotropy Reveals Stress Changes around a Fault as It Is Activated by Hydraulic Fracturing

Nadine Igonin[*,1,2] ⓘ, James P. Verdon[3] ⓘ, and David W. Eaton[2]

Abstract

Subsurface stress conditions evolve in response to earthquakes or fluid injection. Using observations of an induced seismicity sequence from a dense local array, anisotropy analysis is employed to characterize stress changes around a fault. The dataset comprises high signal-to-noise ratio *S*-wave data from 300 events, ranging in magnitude from −0.45 to 4.1, recorded on 98 three-component geophones cemented in shallow wells. It is found that the orientation of the fast *S*-wave direction remains relatively constant for all stations over time, but the magnitude of the anisotropy, as measured by the delay time between the fast and slow *S* wave, exhibits significant local variations. Some stations experience a systematic increase or decrease in the delay time, with a spatial coherence about the injection well. The stress changes due to hydraulic fracturing, aseismic slip, and observed earthquakes are modeled to determine the best fit to the observed anisotropy changes. Our analysis indicates that the creation of a network of tensile hydraulic fractures during fluid injection is likely to be the cause of the observed anisotropy changes. This study confirms that the measurements of seismic anisotropy over time reflects the evolving stress state of a fault prior to and during rupture.

Introduction

Induced seismicity caused by subsurface fluid injection has been generated by a range of industries, including hydraulic fracturing for shale gas (e.g., Bao and Eaton, 2016; Clarke *et al.*, 2019; Verdon and Bommer, 2021), oilfield waste-water disposal (e.g., Ellsworth, 2013), CO_2 sequestration (e.g., Stork *et al.*, 2015), geothermal energy (e.g., Buijze *et al.*, 2019), and natural gas storage (e.g., Ruiz-Barajas *et al.*, 2017). There is a clear and pressing need to better understand the perturbations caused by subsurface injection activities and how these perturbations result in the activation of faults and the occurrence of induced seismicity (Atkinson *et al.*, 2020; Schultz *et al.*, 2020).

Hydraulic fracturing perturbs the state of stress in the subsurface in a number of ways. The elevated pore pressure associated with fluid injection reduces the effective normal stresses, while leaving shear stress essentially unchanged. In low-permeability shale formations, the volume influenced by pore pressure increases is generally limited to a region in close proximity to the injection well, unless pre-existing high-permeability fracture corridors are present to act as a hydraulic conduit (e.g., Riazi and Eaton, 2020; Igonin *et al.*, 2021). By design, the process of hydraulic fracturing creates fractures that open in a tensile manner (mode 1 failure). This tensile opening perturbs the stress field in the surrounding rocks (e.g., Kettlety *et al.*, 2020).

The direct stress changes created by the hydraulic fracturing may cause slip on pre-existing structural features such as natural fractures and faults. This slip may be accommodated as aseismic slip, low-magnitude microseismicity, or larger-magnitude induced seismicity (Eaton, 2018). Slip on pre-existing fractures or faults (whether seismic or aseismic) can create further stress perturbations in the subsurface (e.g., Kettlety *et al.*, 2019), which, in turn, causes additional fault reactivation in a cascading effect (e.g., Eyre, Eaton, Garagash, *et al.*, 2019; Eyre *et al.*, 2020; Peña-Castro *et al.*, 2020).

To date, imaging the relative contributions of these different perturbations has proved challenging. Typically, the locations of observed events are compared with modeled stress perturbations to investigate whether the observed events fall within regions that have experienced positive Coulomb failure stress (ΔCFS),

$$\Delta CFS = \Delta\tau - \mu_f(\Delta\sigma_n - \Delta P), \tag{1}$$

1. Jackson School of Geoscience, University of Texas at Austin, Austin, Texas, U.S.A., ⓘ https://orcid.org/0000-0003-4093-7853 (NI); 2. Department of Geoscience, University of Calgary, Calgary, Alberta, Canada; 3. School of Earth Sciences, University of Bristol, Bristol, United Kingdom, ⓘ https://orcid.org/0000-0002-8410-2703 (JPV)

*Corresponding author: nadine.igonin@austin.utexas.edu

in which $\Delta\tau$ is the change in shear stress, $\Delta\sigma_n$ is the change in normal stress, ΔP is the change in pore pressure, and μ_f is the coefficient of friction (e.g., Stein, 1999; Steacy *et al.*, 2004). However, for hydraulic fracturing cases, the results may be nonunique, making it difficult to fully constrain geomechanical processes associated with fault reactivation and induced seismicity (e.g., Deng *et al.*, 2016; Schultz *et al.*, 2017). Discriminating between different potential fault reactivation mechanisms is of paramount importance because they have differing implications for mitigation. For example, if faults are reactivated by direct pressurization of pore fluids, then an improved understanding of subsurface hydrology is required (e.g., Igonin *et al.*, 2021), whereas if poroelastic stress transfer is the key process causing fault reactivation, then a better understanding of subsurface geomechanics and the relative positions and orientations of wells, hydraulic fractures, and faults may be required (e.g., Kettlety *et al.*, 2020).

To assess the impact of hydraulic fracturing and fault activation on the subsurface stress state, we explore the possibility of using changes in seismic anisotropy. To do so, we use shear-wave splitting (SWS) measurements from microseismic waveforms recorded during stimulation (Verdon *et al.*, 2009). Seismic anisotropy is generated by the alignment of fabrics such as sedimentary layering (e.g., Baird *et al.*, 2017), fracture networks (e.g., Verdon *et al.*, 2009), and stress-induced microcracks (e.g., Verdon *et al.*, 2008) in the subsurface. In the immediate vicinity of rocks where new hydraulic fractures are being created, changes in anisotropy will be driven by the generation of new fracture networks, and SWS observations have been used to image and characterize hydraulic fractures (e.g., Verdon *et al.*, 2010; Wuestefeld *et al.*, 2011; Baird *et al.*, 2013; Verdon and Wuestefeld, 2013; Gajek *et al.*, 2018). Away from the immediate vicinity of the hydraulic fractures, however, we do not expect to see any significant alterations to structural fabrics, so any changes in seismic anisotropy must be driven by changes in the in situ stress field. Such stress changes will act to preferentially open or close microcracks and fractures, leading to changes in the strength and polarization of seismic anisotropy (e.g., Crampin, 1987; Zatsepin and Crampin, 1997; Verdon *et al.*, 2008).

In this study, we analyze the Waskahigan microseismic dataset, which was recorded by a dense surface array deployed to monitor hydraulic fracturing of the Duvernay Shale Formation in the Fox Creek area, Alberta, Canada. In this area, hydraulic fracturing in the Duvernay Shale Formation has generated induced seismicity (e.g., Bao and Eaton, 2016; Igonin *et al.*, 2021), and the regulator has imposed a Traffic Light Protocol for induced seismicity mitigation (Alberta Energy Regulator [AER], 2015). At the site studied here, the largest event reached magnitude M_w 4.1, exceeding the red-light threshold and resulting in the cessation of operations (Eyre, Eaton, Zecevic, *et al.*, 2019). Temporal changes in SWS have

already been observed at the site (Li *et al.*, 2019) using data from four broadband seismograph stations.

We perform SWS measurements on microseismic events observed using a dense surface array of over 90 stations. We find evidence for precursory and coseismic changes in SWS associated with an M_w 4.1 induced event. Some regions experienced an increase in anisotropy strength, whereas other areas experienced a decrease. To interpret our SWS observations, we produce models of the stress perturbations that would be created by different geomechanical processes, including tensile hydraulic fracture opening, microseismic slip on preexisting faults, and aseismic slip on faults. The relative ability of these different mechanisms to account for the observed anisotropy changes provides important inferences with respect to their relative importance in reactivating the fault that produced the M_w 4.1 mainshock.

Dataset

The Waskahigan dataset used in this study is from near Fox Creek, Alberta, where hydraulic fracturing has been conducted in the Devonian-age Duvernay Formation. This site was one of the first in the area to experience an earthquake above magnitude 4.0 (Bao and Eaton, 2016). This dataset has been the focus of several publications (e.g., Wang *et al.*, 2016; Eyre, Eaton, Garagash, *et al.*, 2019; Eyre, Eaton, Zecevic, *et al.*, 2019; Li *et al.*, 2019; Eyre *et al.*, 2020). A dense surface microseismic monitoring array was deployed, providing high-quality microseismic observations that have been used to image fault reactivation by hydraulic fracturing. The largest event (M_w 4.1) occurred on 12 January 2016, during stimulation of the 26th injection stage. This event occurred toward to the heel of the well, as shown in Figure 1. As a result of this event, which exceeded the red-light threshold (Kao *et al.*, 2018), further operations were suspended at this site.

Figure 1a shows the geometry of the seismic monitoring stations in relation to the single well that was completed. At each of the 98 stations, a 4.5 Hz three-component geophone was cemented at the bottom of a 27-m-deep borehole. The average station separation is less than 500 m; this dense station coverage is advantageous for detailed spatial mapping of anisotropy. A study of anisotropy at this site has been performed by Li *et al.* (2019) using data from four broadband seismometer stations (WSK01-04), which are labeled in Figure 1a. The Li *et al.* (2019) results are further examined in the Discussion section.

The shallow borehole array was active for 17 days, from 29 December 2015, to 16 January 2016. A catalog processed by a commercial contractor identified 9769 microseismic events that occurred during that period (Fig. 1). A limited amount of operational microseismicity (i.e., generally weak, M_w <0 event clouds that align with hydraulic fractures) was observed. The bulk of the observed seismicity was associated with the activation of a complex fault structure to the east of the well. Several fault strands can be identified by examining lineations
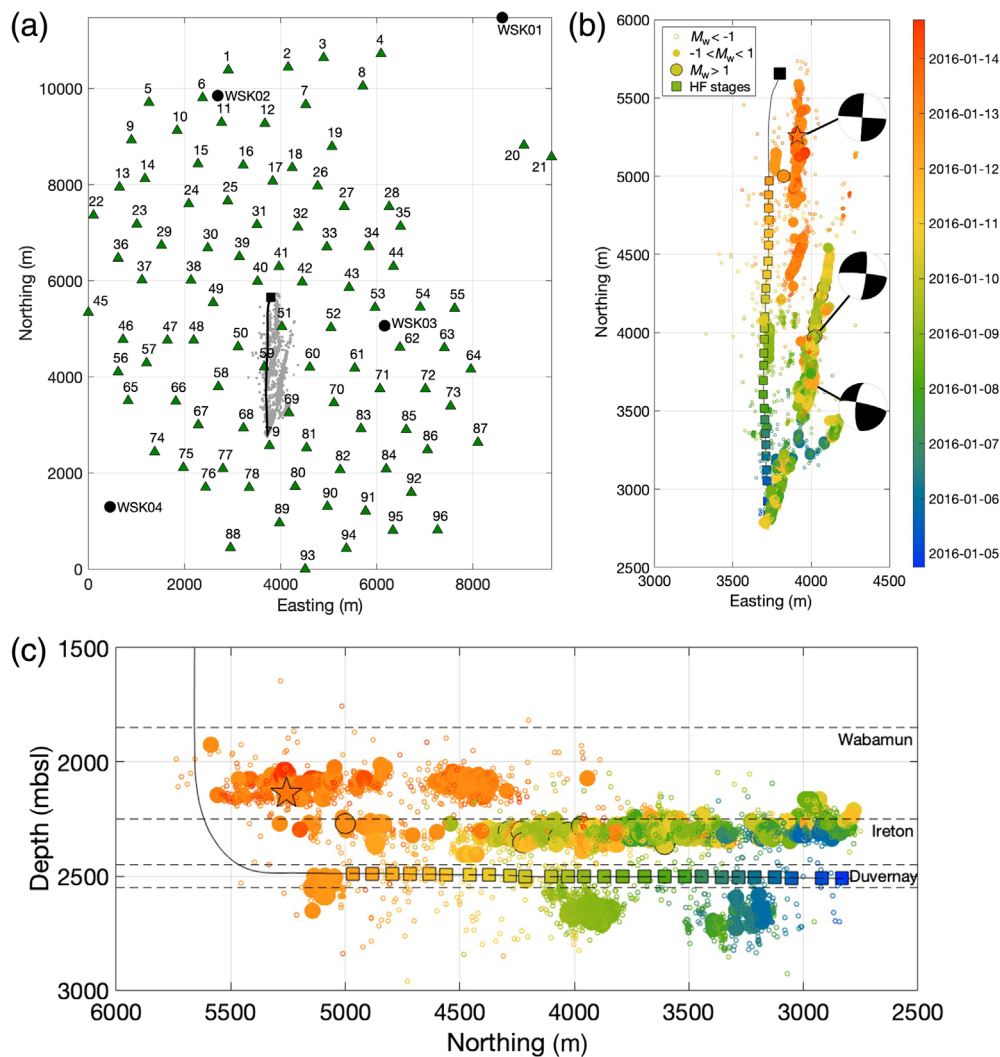
Figure 1. The Waskahigan microseismic dataset. (a) A map of the well (black square and line), geophone locations (green triangles), broadband seismometer stations (black circles) and events (gray dots). (b) A map of the recorded events, showing event locations (circles colored by occurrence time and sized by magnitude) and locations of each injection stage (squares colored by the start time of each stage) along the well (black line). The hypocenter of the M_w 4.1 event is shown by the star. The focal mechanisms for the three largest events are also shown (Wang *et al.*, 2017). (c) A cross section of event and injection stage locations. The approximate depths of the Duvernay, Ireton, and Wabamun Formations are marked by the black dashed lines. The color version of this figure is available only in the electronic edition.

revealed by the microseismic event locations. In particular, a trend of events beginning near the toe of the well, and extending approximately 1.7 km in a north-northeast direction, represents the first structure to activate. A second fault structure, with a north–south strike, can be seen toward the heel of the well, on which the M_w 4.1 mainshock occurred. The focal mechanisms for the three largest events (M_w 2.2, M_w 2.6, and M_w 4.1) can be seen in Figure 1b, and they are right-lateral strike-slip mechanisms for which the primary nodal plane aligns with the first and second fault structures. A number of smaller structures can also be identified. Much of the reactivated fault

structures, as imaged by the microseismicity, occurred in the Ireton and Wabamun Formations, which overly the Duvernay. The faults imaged by the microseismicity are consistent with faults imaged by reflection seismic surveys at the site (Eyre, Eaton, Garagash, *et al.*, 2019). The regional stress field in this area is characterized by $S_{H\,\max}$ orientation that is approximately northeast–southwest (045°), but some local variability in this orientation has been observed (e.g., Igonin *et al.*, 2021).

Eyre, Eaton, Garagash, *et al.* (2019) studied the microseismicity at this site and noted that the bulk of the seismicity was observed in the strata overlying the Duvernay Formation, with gaps in the microseismicity between where stimulation was taking place and where the resulting seismicity was observed. The faults on which the seismicity occurred were observed in the 3D reflection seismic data to extend through the Duvernay into the overlying strata. They inferred that the depth gap in microseismicity was generated by aseismic slip of the fault strands within the Duvernay Formation, with this aseismic slip then promoting seismic ruptures in the overlying Ireton and Wabamun Formations. Eyre, Eaton, Garagash, *et al.* (2019) argued that this aseismic slip outpaced the impacts of direct pore pressure communication along the faults. However, they did not examine any of the other potential mechanisms for generating fault slip that we describe earlier, and they did not present any independent observations to show whether or not this aseismic slip did take place.

SWS Analysis

When a shear wave passes through an anisotropic material, it is split into orthogonally polarized waves that travel with different velocities. This SWS is typically characterized by measurements of the delay time between the fast and slow waves δt and
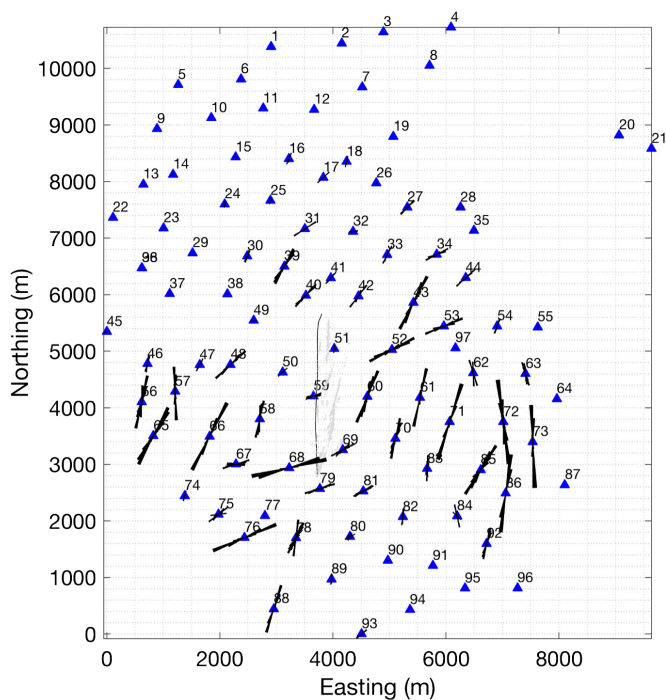
Figure 2. Map of fast *S*-wave polarization direction at each station. Rose diagrams show values of anisotropy orientation, binned at 5° increments. The size of the rose diagrams denotes the number of measurements at each station, with many of the distal stations having no results that passed the quality control criteria. The color version of this figure is available only in the electronic edition.

the orientation of the fast *S*-wave polarization ψ. The delay time is typically normalized by the *S*-wave path length D and the average *S*-wave velocity along the path V_{Savg}, to give the percentage difference between fast and slow *S*-wave velocities δV_S:

$$\delta V_S = 100 \times \frac{\delta t \times V_{Savg}}{D}. \qquad (2)$$

In this study, we assume a straight-line path from event to receiver when performing the normalization, rather than computing ray-bending effects. The average *S*-wave velocity is calculated for each event and ranges between 1927 and 1965 m/s.

We performed SWS measurements on the recorded horizontal components of particle velocity, using 300 of the largest, highest signal-to-noise ratio events. The smallest event used in the analysis had a magnitude of −0.45. We used the semiautomated multiwindowing method described by Teanby *et al.* (2004) to perform the measurements and to quality control the results. Further details are available in the supplemental material to this article. This procedure produced 5931 good quality SWS measurements from the 28,800 individual event-receiver combinations (300 events × 96 receivers).

Figure 2 shows orientation of ψ for all of the SWS measurements at each station. We find that the results for ψ are very consistent at each station, although there is variability between stations, with ψ generally striking north-northeast–south-southwest, but varying from north–south to east-northeast–west-southwest. We did not observe any significant temporal variations in ψ. The spatial variations in ψ may reflect either local variations in natural fracture orientations or variations in $S_{H\max}$ orientation in response to nearby reefs (just south of the study area) and the faults on which seismicity was observed (Eyre, Eaton, Zecevic, *et al.*, 2019).

In contrast to the ψ measurements, many stations showed clear temporal variations in the path-averaged *S*-wave anisotropy strength δV_S. Examples from four stations are shown in Figure 3. Some stations showed changes in δV_S prior to the M_w 4.1 mainshock, and others showed coseismic changes with the mainshock. Some stations showed δV_S changes both prior to the mainshock and during it. The temporal variations for all of the stations are shown in the supplemental material and discussed further therein. In Figure 4, we plot the overall trends observed for every station. We note clear and coherent spatial distributions of stations that experienced either increases or decreases in δV_S. Both prior to the M_w 4.1 mainshock and during it, stations that experienced an increase is δV_S are found to the north and west of the stimulated region, whereas stations that experienced a decrease in δV_S are found to the south and east of the stimulated region. More stations experienced δV_S changes prior to the M_w 4.1 mainshock than coseismically with it, and in general the δV_S changes prior to the M_w 4.1 event were of larger magnitude than those that occurred coseismically.

Previous observations of temporal SWS changes during hydraulic fracturing have been interpreted with respect to changing structural fabrics created by hydraulic fracture propagation (e.g., Verdon *et al.*, 2010; Baird *et al.*, 2013; Verdon and Wuestefeld, 2013). However, those examples have used downhole receivers placed in the reservoir, such that most of the ray paths were through rocks directly affected by the hydraulic stimulation.

In contrast, for this study, events were monitored with a surface array, so most of the ray path is through the overburden. Moreover, most of the events used in our SWS analysis occurred above the injection zone (the Duvernay Formation) in the Ireton and Wabamum Formations. As such, we do not anticipate the volume of rock through which the seismic waves have passed to have experienced significant changes in structural fabric (i.e., the formation of pervasive new sets of fractures). Since we do not anticipate significant generation of new structural fabrics in the rock volume traversed by the seismic waves, any temporal changes in anisotropy must, by a process of elimination, be caused by modulations of fracture or microcrack densities within the overburden resulting from stress changes produced by deformation within the reservoir
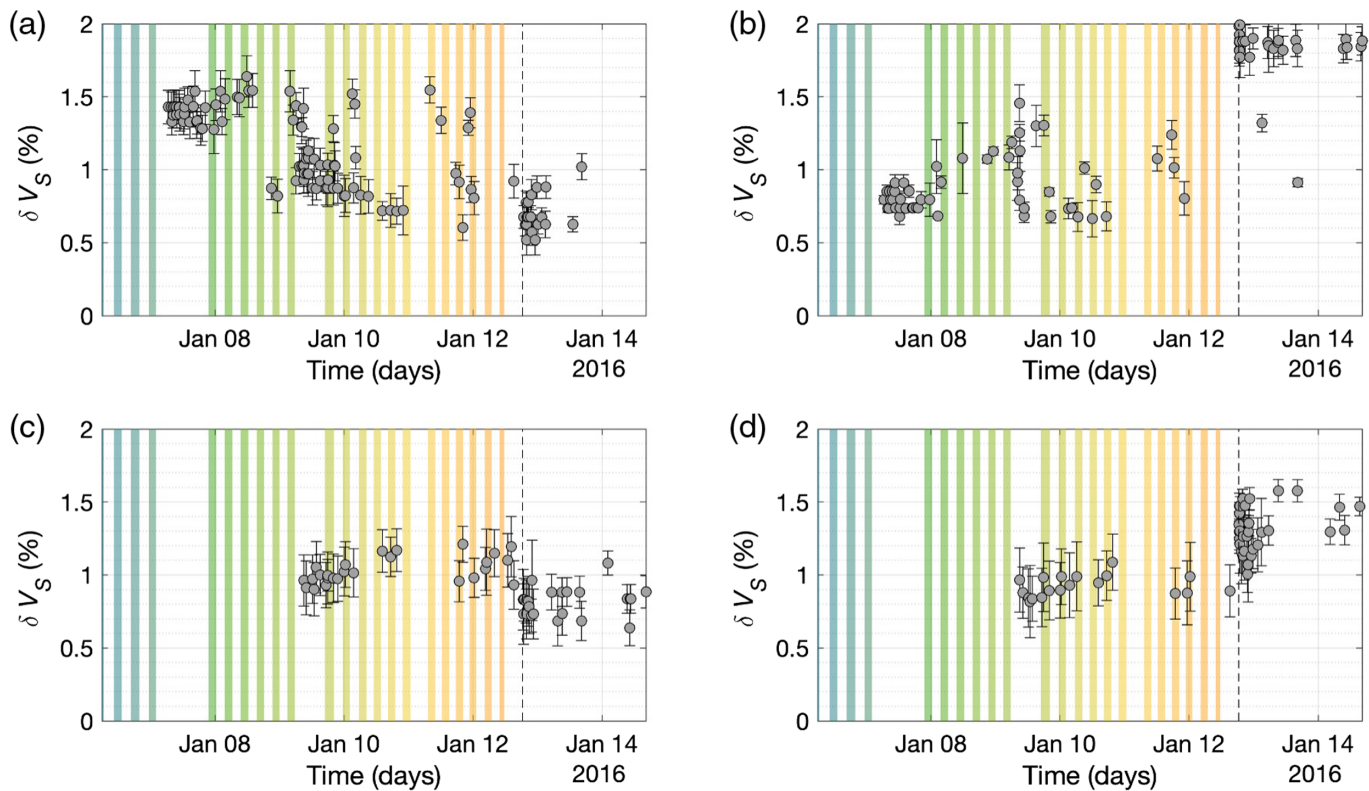
Figure 3. Examples showing stations that experienced temporal changes in δV_S during the stimulation: stations (a) 71, (b) 58, (c) 44, and (d) 34. Stations 71 and 58 experienced increases and decreases in δV_S prior to the M_w 4.1 mainshock on 12 January, whereas stations 34 and 44 experienced increases and decreases in δV_S that were coseismic with the mainshock. The background shaded regions correspond to the times of stages 6–26 and match the color scale in Figure 1. Vertical lines from the measurement points indicate the uncertainty. The color version of this figure is available only in the electronic edition.

and within the overlying fault system. In the following section, we develop deformation models for a selection of different geomechanical processes that may have acted within the reservoir during the hydraulic stimulation to assess the extent to which they may have contributed to the observed SWS changes.
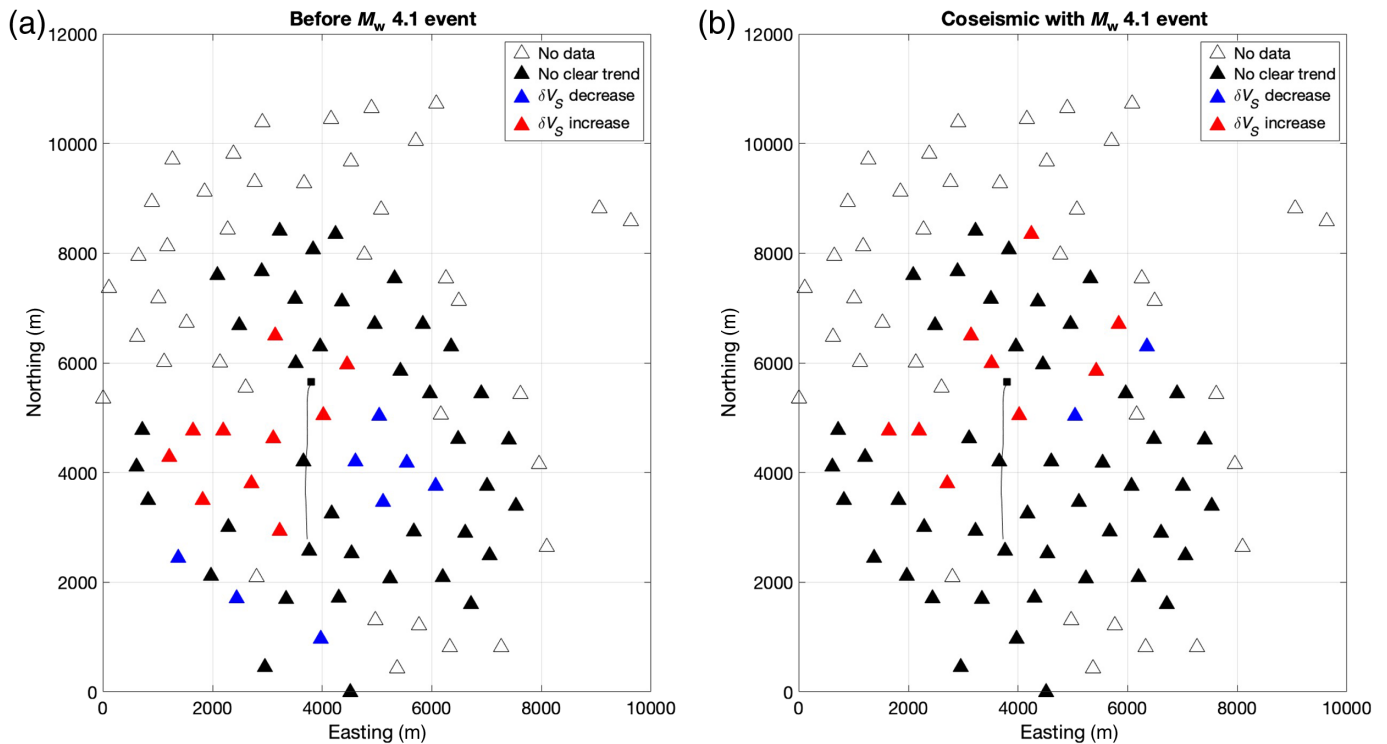
Stress Perturbation Models

We consider five potential sources of stress perturbation that could have created the changes in seismic anisotropy in the layers overlying the reservoir: tensile hydraulic fracture opening, microseismicity, aseismic fault slip, dilatant fault opening, and coseismic slip associated with the M_w 4.1 mainshock event (Table 1). We use the PSCMP code developed by Wang *et al.* (2006), which uses the Okada (1992) equations to model stress perturbations. We compute stress changes throughout the rock volume around the well. In all of the following models, we use Lamé parameters of $\lambda = 25$ GPa and $G = 25$ GPa, and a friction coefficient of $\mu_f = 0.7$, and a Skempton coefficient of 0.4. In the supplemental material, we perform a sensitivity analysis to these parameters and find that the choice of values has little impact on the resulting modeled anisotropy changes.

Tensile hydraulic fracture opening

The tensile opening of hydraulic fractures within the reservoir will generate stress changes in the surrounding rock. In this study, we follow the method described by Kettlety *et al.* (2020) whereby, rather than relying on a single model case for the hydraulic fractures, we stochastically sample the parameters that define hydraulic fracture geometries from appropriate

statistical distributions (as described in the following paragraph), producing 100 such models and computing the median stress changes at each subsurface point. By doing so, we are able to examine the generic impact of tensile hydraulic fracture opening on the surrounding stress field.

In this case, we consider two alternative parameterizations. In the first model, which we refer to as the homogenous HF case (HHF), the hydraulic fracturing from each stage follows identical parameterization, which is based primarily on microseismic observations of hydraulic fracture geometries from other sites within the region. The initiation point for each fracture is positioned relative to the injection point with a normal distribution with a standard deviation of 30 m. Fractures strike in the direction of maximum horizontal stress, either to the northeast (45°) or southwest (235°), with a standard deviation of 5° from these orientations. All of the fractures are vertical. Fracture lengths are selected from a uniform distribution between 0 and 300 m in length and have an aspect ratio
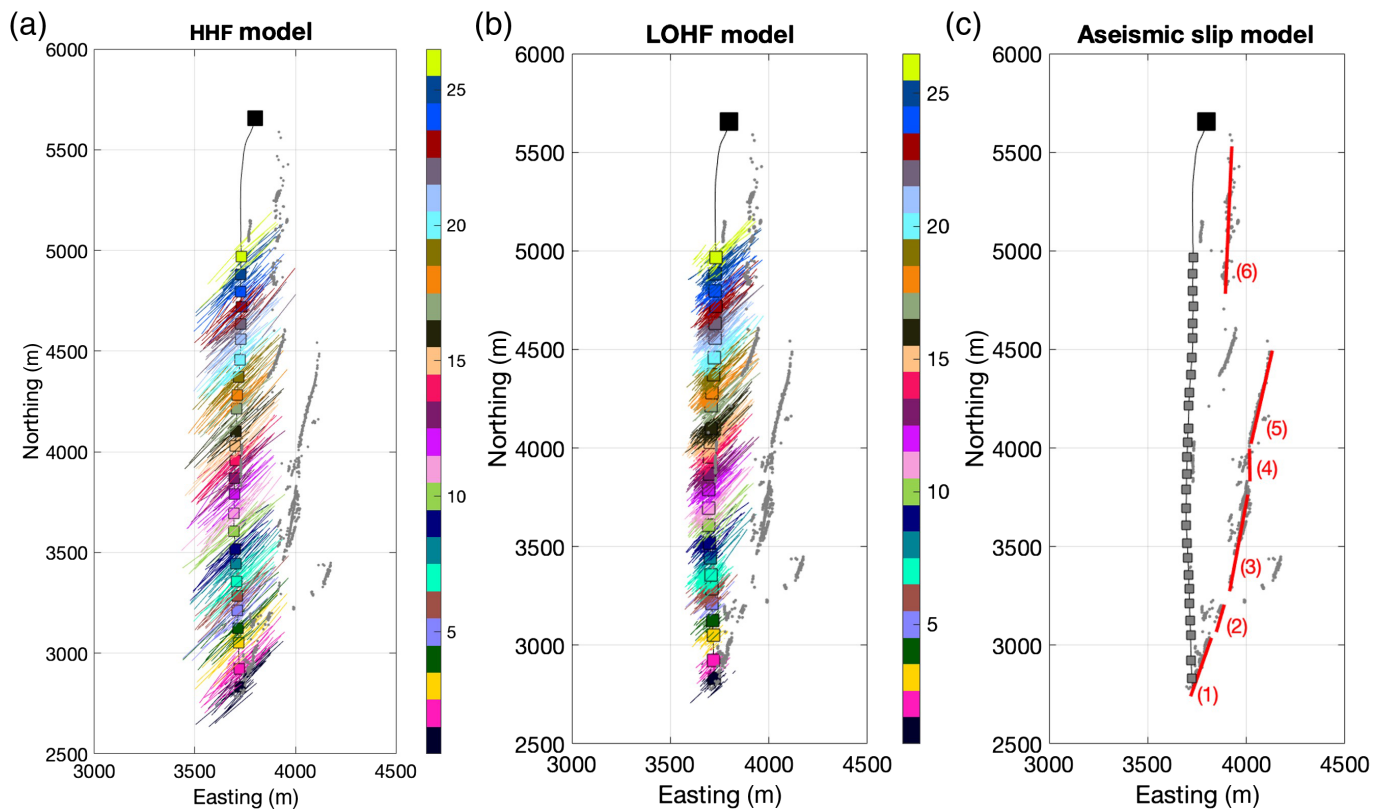
Figure 4. Observed changes in anisotropy strength (δV_S) during stimulation (a) prior to the M_w 4.1 mainshock and (b) coseismic with the mainshock; stations that show a clear increase are plotted in red, those that show a decrease are plotted in blue, stations for which no clear trend was observed are shown in black, and stations for which no shear-wave splitting (SWS) measurements were returned are shown in white. The color version of this figure is available only in the electronic edition.

(i.e., fracture height vs. fracture length) of 0.5. Each fracture accommodates 2 mm of purely tensile opening. The number of fractures is controlled by the injection volume for each stage —we continue to populate fractures according to the aforementioned parameterization until the total volume of the open fractures matches that of the stage injection volume. Figure 5a shows an example hydraulic fracture model generated by this parameterization.

TABLE 1

Summary of the Six Model Scenarios Used to Simulate Stress and Anisotropy Changes around the Waskahigan Wells

Number	Model Name	Model Overview
1	Tensile HF	This model simulates stress changes generated by tensile opening of hydraulic fractures around the well.
2	Tensile HF with leak-off	The same as the prior, but the geometry of tensile hydraulic fractures is adjusted to reflect (1) the predominantly eastward HF propagation and potential limits on HF propagation at the toe of the well due to potential intersection with observed faults.
3	Aseismic fault slip–strike slip	This model simulates aseismic right-lateral slip along the observed northeast-trending fault structures, as postulated by Eyre, Eaton, Garagash, et al. (2019).
4	Observed microseismicity	This model computes stress changes that would be generated by the observed microseismic events, with slip amounts determined by event magnitudes and slip orientations determined by observed source mechanisms.
5	Aseismic fault slip–dilatant	This model simulates aseismic dilation along the observed northeast-trending fault structures; this dilation might be expected as elevated pore pressures in the reservoir intersect the faults.
6	Coseismic with mainshock	This model simulates the coseismic stress changes that would be generated by the M_w 4.1 mainshock. The slip amount is based on the event magnitude, and the slip orientation is based on the observed focal mechanism.

Figure 5. (a) An example of a stochastically generated homogenous HF case (HHF) hydraulic fracture model used to simulate the impacts of tensile fracture opening. In map view, we show the injection points (squares) colored by stage number, with the modeled fractures shown as colored lines extending from each injection point. (b) An example of the alternative leak-off hydraulic fracturing model (LOHF) model, which accounts for the potential impacts of the intersection between hydraulic fractures and the structures at the toe of the well. (c) The positions of the aseismic slip patches (red lines numbered 1–6) used to simulate the stress perturbations created by aseismic slip. Patches 1–5 represent the large north-northeast-trending structure, and patch 6 represents the north–south-striking fault at the heel of the well. In all plots, observed microseismic events with $M_w > -1$ are shown as gray dots. The color version of this figure is available only in the electronic edition.

The majority of the observed microseismicity is found to the east of the well (Fig. 1). Such asymmetric fracture growth is not uncommon and may be driven by gradients in the in situ stress conditions or geomechanical properties (e.g., Maxwell and Norton, 2012). The early stages at the toe of the well would have immediately intersected the large, north-northeast-trending structure. We might expect the intersection with this structure to have limited the length of the resulting hydraulic fractures and potentially have allowed significant volumes of fluid leak-off to take place. We therefore adjusted our HHF model to take these factors into consideration. In the leak-off hydraulic fracturing model (LOHF), the asymmetry in hydraulic fracture propagation direction is recognized by assigning a 75% probability that a given HF will propagate to the northeast (and a 25% probability of striking to the southwest). All fractures that strike to the southwest have a maximum length of 100 m. For the first seven stages, fractures that strike to the northeast have a maximum length of $L_{MAX} = [50, 55, 60, 65, 100, 100, 100]$, respectively. All subsequent stages have $L_{MAX} = 300$ m. For the first 10 stages, the effective fluid injection volumes, which we use to define the total number of hydraulic fractures as described earlier, is reduced by the following leak-off fractions $F_{LO} = [0.1, 0.1, 0.1, 0.1, 0.1, 0.5, 0.5, 0.5, 0.5, 0.5]$. Figure 5b shows an example hydraulic fracture model generated by this parameterization; the resulting modeled hydraulic fractures are constrained such that they do not cross the large north-northeast-trending structure imaged by the microseismicity.

Microseismicity

The observed microseismicity, which in this case primarily represents shear slip on pre-existing faults and fractures, will create stress changes in the surrounding rocks. The microseismic contractor who processed these events computed source mechanisms for every identified event. For this study, we only utilize events with magnitudes greater than −1.0 because these are more likely to have robust focal mechanisms. Because deformation will scale with magnitude, they represent the largest potential sources of deformation. We examine the coseismic effects of the M_w 4.1 mainshock separately (see subsequently), so for the microseismicity we only consider events

prior to the mainshock. Each event is treated as a square slip patch centered on the event hypocenter. The strike, dip, and rake for each event are determined from the source mechanisms. We do not have any independent measurement of the rupture area or slip amount. We therefore assume that each event has a stress drop of $\Delta\sigma = 1$ MPa (we show the impact of using different $\Delta\sigma$ values in the supplemental material), with the rupture area A then determined by the seismic moment M_0 (Kanamori and Brodsky, 2004):

$$A = \left(\frac{M_0}{\Delta\sigma}\right)^{\frac{2}{3}}, \tag{3}$$

and slip d given by

$$d = \frac{M_0}{GA}. \tag{4}$$

Aseismic slip

As described earlier, the lack of seismicity within the Duvernay Formation itself, in comparison with the numbers of events located in the overlying Ireton and Wabamun Formations, led Eyre, Eaton, Garagash, et al. (2019) to interpret that the mainshock was triggered by a process of aseismic slip. We therefore generate stress transfer models to evaluate this hypothesis. Based on the microseismic observations, we simulate aseismic slip on two structures—the large, approximately 1.7-km-long, north-northeast-trending structure that reactivated near the toe of the well and the north–south-trending fault toward the heel of the well on which the mainshock is located. We define five aseismic slip patches along the north-northeast-trending structure (numbered 1–5 in Fig. 5c) and a single slip patch along the north–south-trending fault (numbered 6 in Fig. 5c). Following the aseismic slip model presented by Eyre, Eaton, Garagash, et al. (2019), we assume that each aseismic slip patch extends from 2700 to 2300 mbsl (meters below sea level) depth and that 2 cm of right-lateral slip occurs on each patch during stimulation.

In addition to aseismic strike-slip motion on these faults, the increased pore pressure within the reservoir could have created dilatant motion. We therefore generated an additional model to simulate this process. The same slip patches as shown in Figure 5c were used. Because the models developed by Eyre, Eaton, Garagash, et al. (2019) showed that pore pressures would not extend as far along the faults as the aseismic slip, we modeled the dilatant slip as extending from 2600 to 2400 mbsl, with 2 cm of tensile opening taking place.

M_w 4.1 mainshock

Since some stations showed a change in anisotropy that is coseismic with the M_w 4.1 mainshock, we also compute the stress perturbations that would be created by this event. We

follow the same procedure as described earlier for the microseismic events to compute the position, dimensions, and slip amount for this event (equations 3, 4). For the source mechanism of this event, we use the inversion results of Wang et al. (2016), who estimated a strike, dip, and rake of 184°, 82°, and 166°, respectively.

Stress changes and anisotropy

For all of the models described earlier, we use the PSCMP code (Wang et al., 2006) to compute the stress perturbations in the reservoir and surrounding rocks. To make comparisons between the models and the observed anisotropy, we need to consider the impact of stress changes on seismic velocities. In general, increases in compressive stress will produce increases in seismic velocity, for both fractures and grain-boundary microcracks are forced closed (e.g., Verdon et al., 2008). Increases in compressive stress will reduce seismic anisotropy because it is the alignment of these fractures and microcracks that creates anisotropy in sedimentary rocks. In the following results, we map changes in the mean of the principal stresses Δp:

$$\Delta p = \frac{\Delta\sigma_1 + \Delta\sigma_2 + \Delta\sigma_3}{3}, \tag{5}$$

in which $\Delta\sigma_{1,2,3}$ are the principal components of the change in stress generated by the PSCMP code, positive Δp denotes a reduction in compressive stress, and negative Δp denotes an increase in compressive stress. We consider the mean principal stress change because an increase in compressive stress will serve to close cracks and fractures regardless of their orientation, thereby reducing the anisotropy, whereas a decrease in compressive stresses will allow cracks and fractures to open, thereby increasing anisotropy.

The net change in anisotropy measured at a given station will be determined by overall changes along the ray paths traveled to each station. We consider straight line paths from putative event locations within microseismic events to each receiver. For the ray path to each station, we compute the mean value of Δp along this path. We then compare the modeled changes in stress along given ray paths with the observed changes in anisotropy.

Results

In Figure 6, we plot maps and cross sections of the stress changes produced by each of the models described earlier. The maps are plotted at a depth of 2100 mbsl because this represents a depth through which most of the observed ray paths traveled, whereas the cross sections are plotted through the center of the microseismic cloud. We find that the aseismic slip patch and microseismic event models produce similar results, with lobes of increased compressive stress to the northwest and southeast of the stimulated zone and lobes of reduced
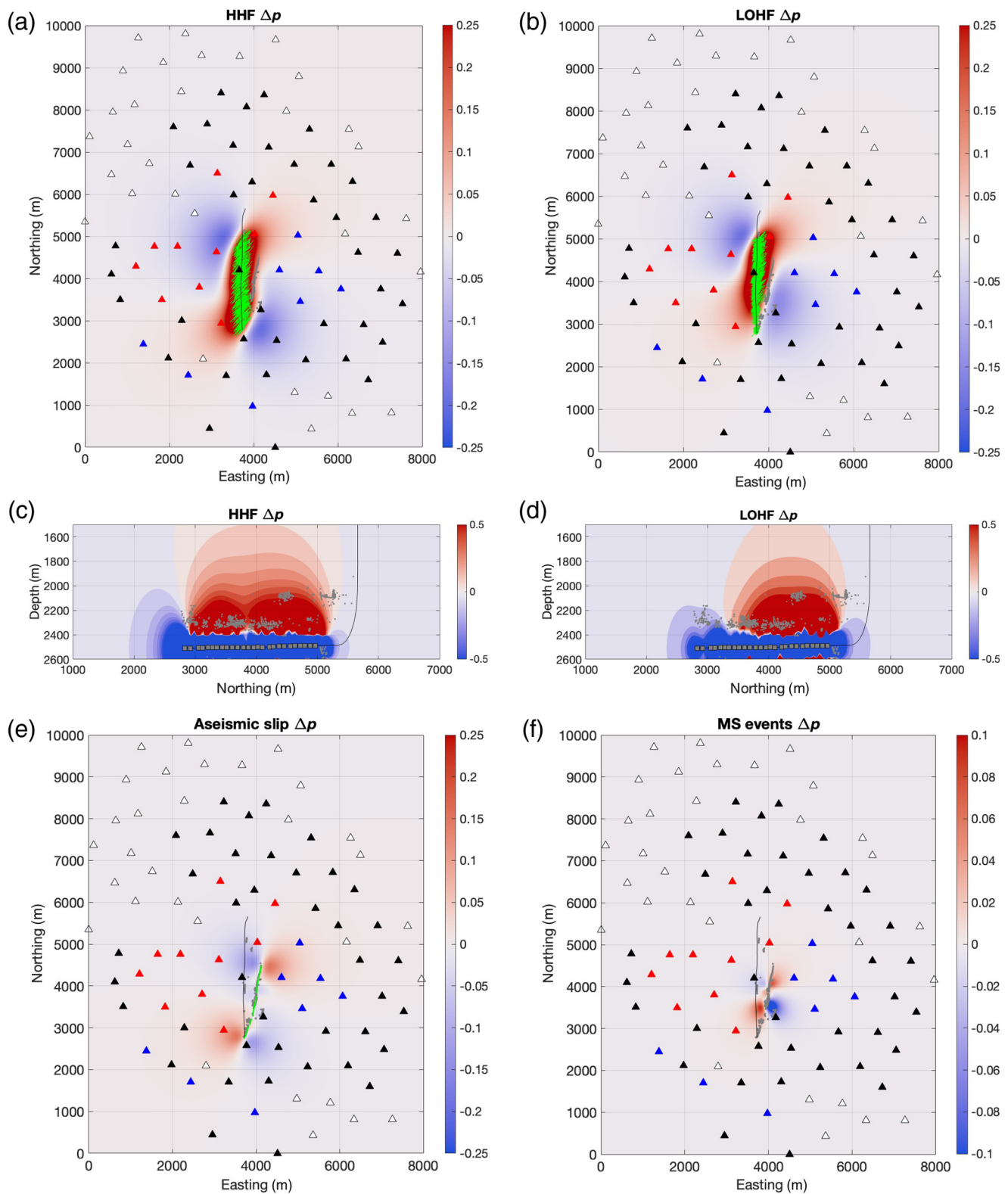
Figure 6. (a,b,e,f,i,k) Maps and (c,d,g,h,j,l) cross sections showing the changes in mean principal stress, Δ*p* (in MPa), generated by the (a,c) HHF, (b,d) LOHF, (e,g) aseismic slip, (f,h) microseismic slip, (i,j) dilatant fault slip, and (k,l) coseismic slip with the M_w 4.1 mainshock models. The maps show the stress changes at a depth of 2100 mbsl, and the cross sections are plotted along a line of *y* = 3825 m. In the map plots, the locations of monitoring stations are shown and colored by the observed temporal changes in SWS prior to the (a,b,e,f,i) M_w 4.1 mainshock and the (k) M_w 4.1 coseismic changes, as per Figure 4. Microseismic event locations are shown with gray dots, and the well is shown with a black solid line. The color version of this figure is available only in the electronic edition. (*Continued*)
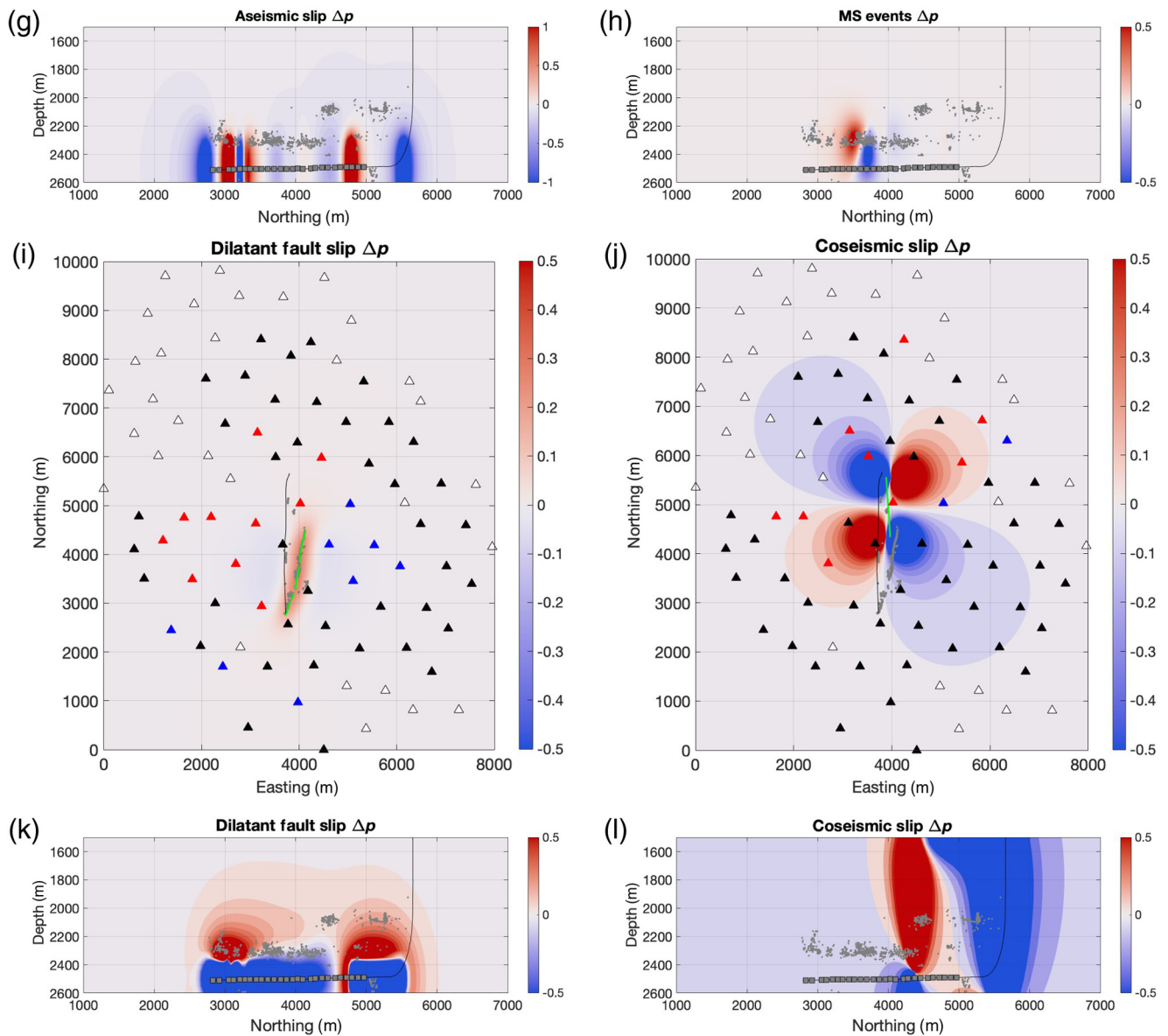
Figure 6. Continued

compressive stress to the southwest and northeast of the stimulated zone. The stress changes from the aseismic slip model are generally larger than those produced by the microseismic events. The dilatant fault-slip model produces a zone of reduced compressive stresses above the fault, with smaller zones of increased compressive stress to the east and west.

The results from the two tensile hydraulic fracture opening models are similar to each other and very different from the aseismic slip, microseismicity, and dilatant fault-slip results. The hydraulic fracture models have reduced compressive stresses in the region overlying the hydraulic fractures and increased compressive stresses in the regions to the northwest and southeast. The coseismic slip model produces lobes of

increased compressive stress to the northwest and southeast of the mainshock location and decreased compressive stress to the northeast and southwest. The coseismic stress changes are large but more spatially limited in extent than the changes produced by the other models.

Figure 7 shows the resulting modeled stress changes along the ray paths to each receiver. For the hydraulic fracturing, aseismic slip, dilatant fault slip, and microseismic models, we compute stress changes along ray paths originating at $x = 3925$ m, $y = 3635$ m, $z = 2300$ mbsl, in the center of the cloud of microseismic events that occurred before the mainshock. After the mainshock, the loci of microseismicity shifted onto the northernmost fault strand, so for the coseismic model we
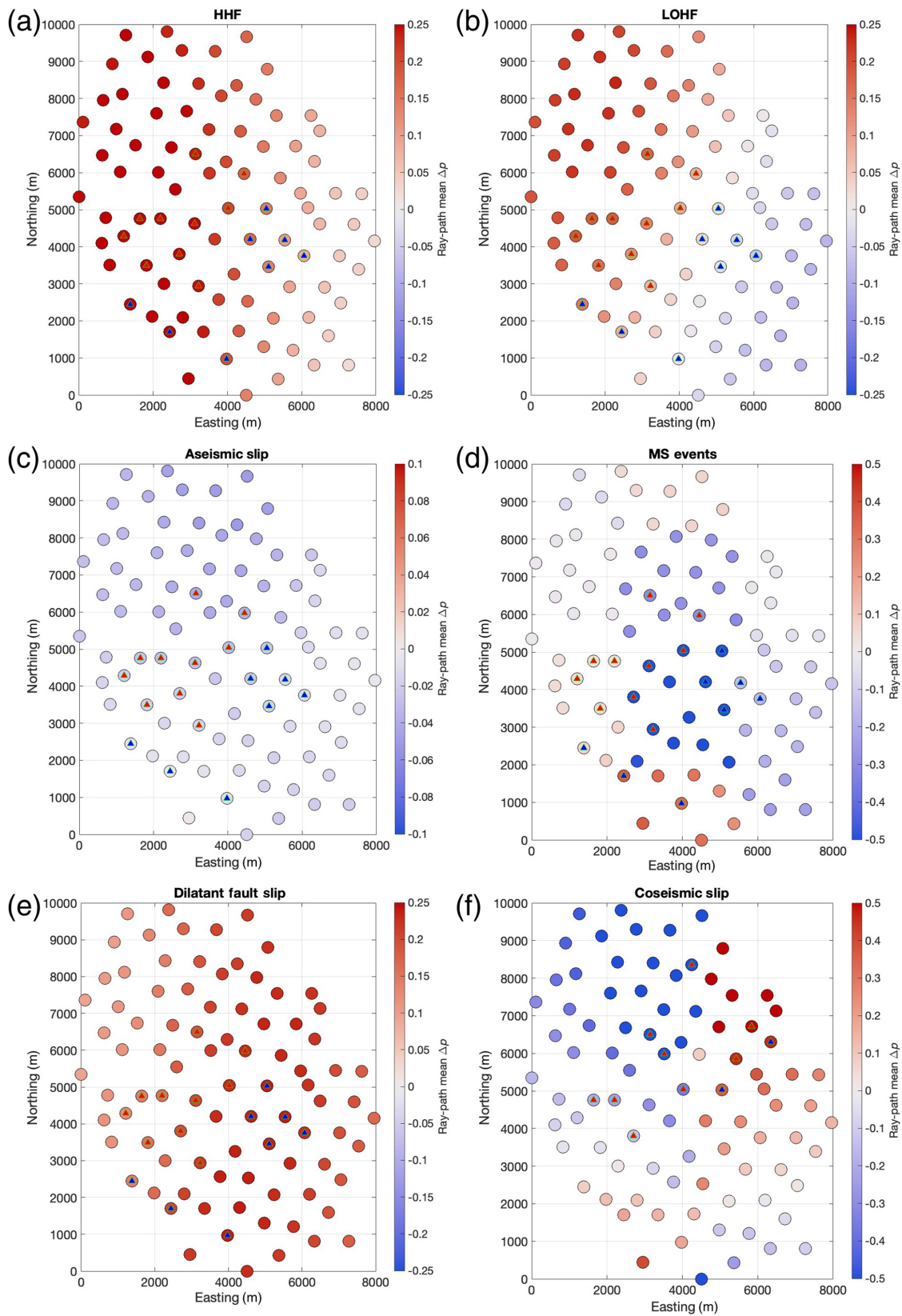
Figure 7. Average Δp along the ray paths to each station (colored circles) for each stress model: (a) HHF, (b) LOHF, (c) aseismic slip, (d) microseismic events, (e) dilatant fault slip, and (f) coseismic slip. We also plot the observed changes in δV_S for stations at which a measurable trend was observed (triangles within the colored circles) as per Figure 4. The color version of this figure is available only in the electronic edition.

plot the stress changes along ray paths originating at $x = 3925$ m, $y = 5135$ m, $z = 2100$ mbsl.

The model results presented in Figure 7 allow us to make direct comparisons with the observed δV_S changes at each station. Prior to the occurrence of the M_w 4.1 mainshock, we observed increases in δV_S for stations to the north and west of the well and decreases in δV_S for stations to the south and east of the well.

The aseismic slip patch model produces relatively small Δp changes in the rocks above the reservoir, and the mean changes in Δp are negative along the ray paths to all stations. Conversely, the dilatant fault-slip model and the homogenous hydraulic fracturing model both produce mean changes in Δp that are positive along the ray paths to all stations. Given that the observed anisotropy increases along some ray paths and decreases along others, these models struggle to account for the observed trends in increasing and decreasing δV_S.

The microseismic event model produces a more complicated pattern of negative and positive mean Δp changes, with negative values for receivers close to the well and to the north and positive values for stations to the south and east. Again, however, this model does not match the trends in δV_S that we observed.

The LOHF model, which accounts for potential fault intersections and leak-off in the growth of hydraulic fractures, produces a pattern of mean Δp changes that has positive values for stations to the north and west of the well and negative values for stations to the south and east. This broadly matches the pattern of δV_S changes that we observed. It is therefore reasonable to surmise that the changes in anisotropy that we observed prior to the occurrence of the M_w 4.1 mainshock are consistent with the stress changes that would be produced in the overburden by tensile opening of hydraulic fractures in the reservoir, as long as the hydraulic fractures at the toe of the well are limited by their interaction with the fault, which has been mapped by both microseismic and 3D reflection seismic observations.

Figure 7e compares the modeled Δp changes along ray paths to every station with the observed changes in δV_S coseismic with the mainshock. The model produces positive changes in Δp for stations to the northeast and southwest of the well and negative changes in Δp for stations to the northwest and southeast of the well. This does not match the observed coseismic δV_S changes, which have a similar pattern to the δV_S changes observed prior to the mainshock, with increases in δV_S to the northwest of the well. In fact, the hydraulic fracturing models, and in particular the LOHF model, produce modeled Δp changes that provide the closest match to the δV_S observations. We therefore suggest that the coseismic δV_S observations do not represent a substantial change in deformation produced by the M_w 4.1 event, but they simply represent a continuation of the deformation produced by the propagation of hydraulic fractures.

In the following section, we explore the implications of the observed anisotropy trends and how they can be used to potentially distinguish between different triggering mechanisms. We also discuss the temporal anisotropy results and interpretations of Li *et al.* as compared with the results shown in this article. Finally, we conclude with a short discussion on how SWS observations can be used in the monitoring of injection induced seismicity.

Discussion
Implications for fault reactivation mechanisms
As described earlier, Eyre, Eaton, Garagash, *et al.* (2019) proposed a model for fault reactivation whereby aseismic slip on faults in the reservoir is the driving force in reactivating the faults, leading to the M_w 4.1 mainshock. However, they did not investigate alternative potential triggering mechanisms. The modeling work presented here suggests that the observed changes in seismic anisotropy are most consistent with the stress changes in the overburden that would be generated by tensile opening of hydraulic fractures. It is therefore of interest to compare the fault reactivation potential for the hydraulic fracturing and aseismic slip patch models.

Fault reactivation due to subsurface stress changes is typically considered within the framework of perturbations in the ΔCFS (equation 1). A positive ΔCFS implies that conditions on a fault have moved toward the failure envelope, increasing the likelihood that slip will occur, whereas a negative ΔCFS implies a move away from failure conditions. Hence, perturbations that create significant positive changes in ΔCFS can be thought of as representing plausible mechanisms for generating induced seismicity.

In Figure 8 we plot the ΔCFS, as resolved onto the M_w 4.1 mainshock fault plane, produced by the LOHF and aseismic slip models. The ΔCFS maps are plotted at 2130 mbsl, the depth of the mainshock hypocenter. Both models produce positive ΔCFS changes at the mainshock hypocenter prior to its occurrence, indicating that both mechanisms represent potential causal mechanisms for triggering the induced seismicity. A wide range of ΔCFS values have been invoked as being necessary to reactivate faults, from 0.001 to 0.5 MPa (e.g., Kilb *et al.*, 2002; Freed, 2005; Shapiro *et al.*, 2006). The 0.15 < MPa < 0.3 MPa ΔCFS changes produced by both models are above triggering thresholds that have previously been invoked to account for fault reactivation during hydraulic fracturing (e.g., Deng *et al.*, 2016; Kettlety *et al.*, 2019, 2020).

We further investigate the plausibility of both potential mechanisms by evaluating the temporal evolution ΔCFS produced by each model. For the tensile hydraulic fracture LOHF model, we simulate the cumulative ΔCFS at the mainshock hypocenter as each stage is emplaced. To assess the temporal evolution of ΔCFS for the aseismic slip model, we assume that slip on patches 1–5 (see Fig. 5c) occurs at a constant rate during stimulation of stages 1–22 and that slip on patch 6 occurs at a constant rate during stimulation of stages 23–26.
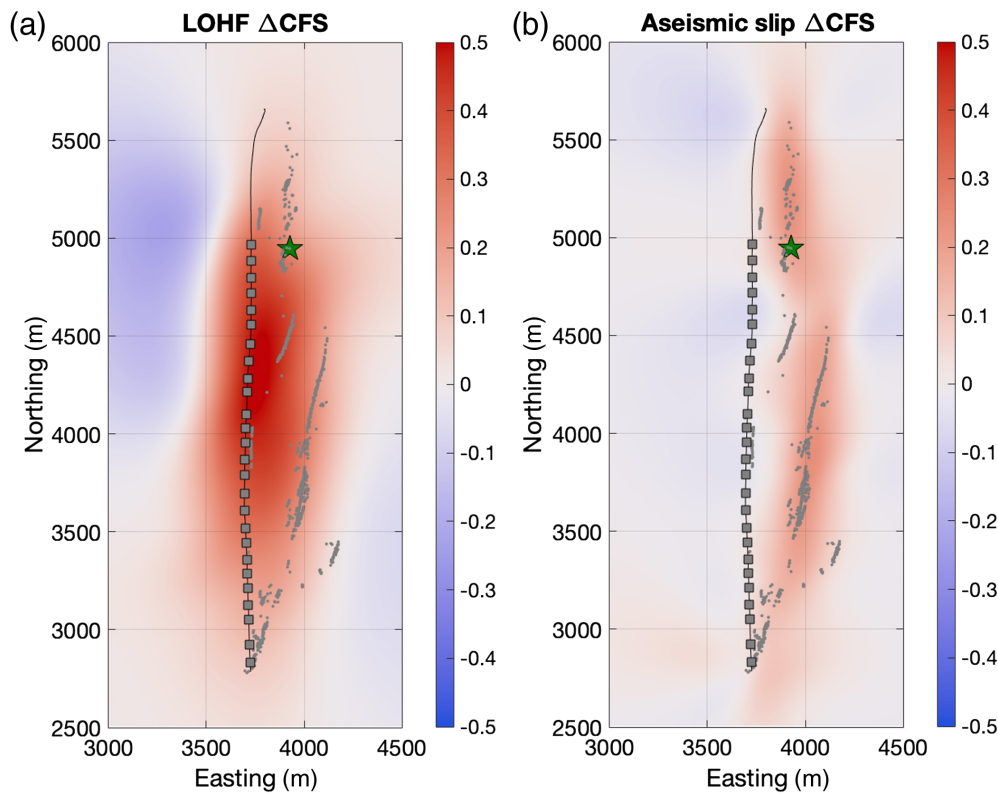
Figure 8. Modeled Coulomb failure stress (ΔCFS) changes produced by (a) tensile opening of hydraulic fractures (LOHF model) and (b) aseismic slip patches, plotted at the depth of the M_w 4.1 mainshock. The mainshock location is marked by the green star. The well and injection points are marked (black line and gray squares), as are the positions of all $M_w > -1$ events (gray dots). The color version of this figure is available only in the electronic edition.
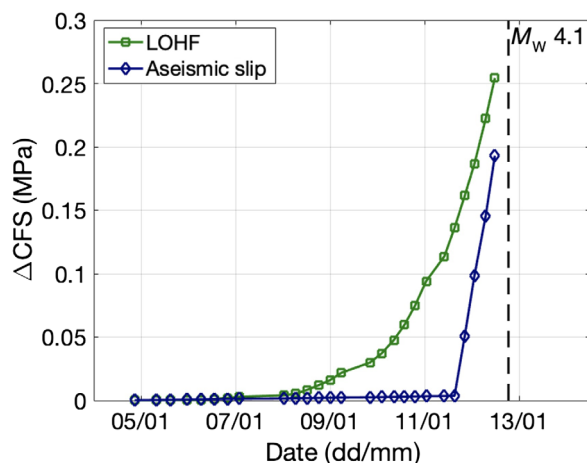
Figure 9. Modeled temporal evolution of ΔCFS at the M_w 4.1 mainshock hypocenter, prior to the occurrence of this event, as generated by the tensile hydraulic fracture LOHF model (green squares) and the aseismic slip model (blue diamonds). The symbols along each curve are placed at the start time of each fracturing stage (from 1 to 26). The timing of the mainshock is shown by the vertical dashed line. The color version of this figure is available only in the electronic edition.

Figure 9 shows the modeled temporal evolution of ΔCFS at the mainshock hypocenter. Both models produce small ΔCFS changes during the early stages of stimulation, with ΔCFS increasing sharply in the 24 hr prior to the mainshock. Hence, the modeled temporal evolutions of ΔCFS produced both by the tensile hydraulic fracture opening and the aseismic slip patch models are consistent with the timing of the M_w 4.1 mainshock.

Hence, with respect to the timing and magnitude of ΔCFS changes produced on the fault responsible for the M_w 4.1 mainshock, both aseismic slip on reservoir faults (as proposed by Eyre, Eaton, Garagash, *et al.*, 2019) and stress changes produced by tensile hydraulic fracturing are plausible candidates for generating the induced seismicity that was observed at this site. In the absence of further geophysical observations, it would be challenging to further discriminate between the relative importance of these two phenomena. However, as shown in Figure 7, the overburden stress changes from the tensile hydraulic fracture model produce a much better match to the observed seismic anisotropy changes than do the overburden stress changes from the aseismic slip model. As such, this indicates that the stress changes from tensile hydraulic fracture opening were the dominant process affecting rocks in the overburden and were therefore the predominant cause of the fault reactivation. However, in making this conclusion, it is entirely plausible that several factors including stress changes from tensile hydraulic fracture opening, aseismic slip on reservoir faults, and indeed pore pressure migration along faults (e.g., Igonin *et al.*, 2021) could all have jointly contributed to the fault reactivation that produced the M_w 4.1 mainshock.

Li *et al.* (2019)

Li *et al.* (2019) performed a study of changes in seismic anisotropy using data recorded by four broadband seismometers that were also deployed at this site (Fig. 1). They found that the main temporal change in the anisotropy occurred after the M_w 4.1 mainshock, and they hypothesized that the SWS changes were generated by a loss of fluids from the hydraulic

fracture system into the fault, which caused the hydraulic fractures to close. However, the small number of stations used by Li *et al.* limits the number of measurement points used in their analysis. Of the four broadband stations, WSK01 was discarded by Li *et al.* as being beyond the shear-wave window (Booth and Crampin, 1985). Stations WSK02 and WSK04 are more than 4 km laterally from the well, and the events are located at a depth below ground of approximately 3 km, so it is difficult to determine if these stations are within the shear-wave window. The results obtained by Li *et al.* (2019) did not show any temporal changes at stations WSK02 and WSK03, and the only evidence for any temporal change found by Li *et al.* (2019) came from six measurements made at station WSK04. However, these temporal changes were associated with different clusters of events, and their method did not account for normalizing the observed delay times by path length. As such, it is unclear whether the changes that they observed actually represent a change in anisotropy or simply a change in the loci of events used to make the measurements because a change in path length will produce a change in δt even if there is no change in the strength of the anisotropy. For this reason, we stress the importance of normalization in our results.

With respect to the physical mechanism proposed by Li *et al.* (2019), the microseismic events on which SWS measurements were made are located in the overlying Ireton and Wabamun Formations, with an upward ray path to the near-surface stations. As such, no part of the ray path could have sampled the reservoir, so any changes in anisotropy cannot have been generated directly by hydraulic fractures themselves (except through the impact of the stress changes that they might generate in overlying strata, as we have demonstrated). As such, the hypothesis proposed Li *et al.* (2019) may not be plausible.

We proposed and tested several hypotheses in our study because we were able to make use of thousands of SWS measurements recorded on a dense surface array, which affords us the resolution to investigate in detail the spatial and temporal changes in anisotropy. Although we have observed some changes in anisotropy at some stations associated with the M_w 4.1 mainshock, we show that many stations showed a gradual temporal evolution through time as the hydraulic fracturing progressed, prior to the occurrence of the mainshock. Similarly, the dense spatial coverage has allowed us to characterize the spatial distribution of anisotropy changes, with some regions experiencing increases in anisotropy and others experiencing decreases at the same time. Such changes cannot be accounted for by the Li *et al.* fracture closure model; however, as we have demonstrated, they are entirely consistent with the stress changes that we would expect to occur around and above tensile-opening hydraulic fractures.

Implications for injection induced seismicity

To date, SWS measurements on microseismic datasets during hydraulic fracturing have primarily been performed using downhole monitoring arrays placed in or near the reservoir. As such, ray paths are predominantly through reservoir rocks, allowing us to directly image sedimentary structures (e.g., Baird *et al.*, 2017) and fracturing (e.g., Verdon *et al.*, 2010; Wuestefeld *et al.*, 2011; Baird *et al.*, 2013; Verdon and Wuestefeld, 2013; Gajek *et al.*, 2018) within the reservoir.

For microseismic datasets recorded using surface arrays, the majority of the ray path is through the overburden, meaning that we cannot directly image hydraulic fractures within the reservoir. However, this study shows that measurements of SWS made using dense surface arrays can still provide useful information with respect to geomechanical processes occurring within the reservoir. The fact that the LOHF model, which incorporates the effects of leak-off and limitations in HF length, produces a better match to the observed SWS than the HHF model, which does not, provides independent evidence for the interaction between the hydraulic fractures and the fault. Similarly, we have shown that different geomechanical processes occurring within the reservoir produce very different patterns of stress change that extend into the overburden, and the relative importance of these different processes can therefore be distinguished through careful observations of SWS changes made using dense surface arrays.

Although the results in this article are related specifically to hydraulic fracturing, these methods can also be used for interpreting seismicity due to wastewater injection or carbon capture and sequestration. Since both of these processes change the subsurface stress conditions, it is possible that these changes can be monitored using SWS measurements over time.

Conclusions

The process of hydraulic fracturing perturbs the stress field in the target reservoir and the rocks that surround it. These perturbations can reactivate pre-existing faults, leading to induced seismicity. The occurrence of induced seismicity has posed a challenge for operations in several important shale gas plays around the world. Methods to image the stress perturbations created by hydraulic fracturing are of key importance to better understanding these geomechanical processes. In this study, we have performed measurements of seismic anisotropy using SWS recorded by a dense surface monitoring array deployed above a hydraulic fracturing site in the Fox Creek region of Alberta, Canada. An M_w 4.1 event was triggered at this site, which caused the shut down of the operation.

We observed clear and coherent temporal changes in SWS during the hydraulic fracturing process. Given that the recorded ray paths traveled almost exclusively through the overburden, stress changes generated by hydraulic fracturing are the most plausible driver of the temporal anisotropy variations. We developed several candidate models to simulate stress perturbations around the reservoir, including tensile hydraulic fracturing, microseismic slip on faults, aseismic slip on faults, and coseismic slip with the M_w 4.1 mainshock. We

also developed a modified hydraulic fracturing model whereby the growth of hydraulic fractures was limited by their intersection with a known, mapped fault. We compared the results of these various models with the observed anisotropy and found that the only case with stress perturbations that matched the positions where increases and decreases in anisotropy were observed was provided by the modified hydraulic fracture model. We then assessed the stress changes produced at the hypocenter of the M_w 4.1 mainshock and found that this model produces significant positive ΔCFS changes at the hypocenter in the 24 hr prior to the event and therefore represents a plausible candidate mechanism for the triggering of this event.

Data and Resources

Declaration of Competing Interests

The authors acknowledge that there are no conflicts of interest recorded.

Acknowledgments

References

Alberta Energy Regulator (AER) (2015). Subsurface Order No. 2, available at https://aer.ca/documents/orders/subsurface-orders/SO2.pdf (last accessed February 2022).

Atkinson, G. M., D. W. Eaton, and N. Igonin (2020). Developments in understanding seismicity triggered by hydraulic fracturing, *Nat. Rev. Earth. Environ.* **1,** 264–277, doi: 10.1038/s43017-020-0049-7.

Baird, A. F., J.-M. Kendall, Q. J. Fisher, and J. Budge (2017). The role of texture, cracks and fractures in highly anisotropic shales, *J. Geophys. Res.* **122,** 10,341–10,351.

Baird, A. F., J.-M. Kendall, J. P. Verdon, A. Wuestefeld, T. E. Noble, Y. Li, M. Dutko, and Q. J. Fisher (2013). Monitoring increases in fracture connectivity during hydraulic stimulations from temporal variations in shear-wave splitting polarization, *Geophys. J. Int.* **195,** 1120–1131.

Bao, X., and D. W. Eaton (2016). Fault activation by hydraulic fracturing in western Canada, *Science* **354,** 1406–1409.

Booth, D. C., and S. Crampin (1985). Shear-wave polarizations on a curved wavefront at an isotropic free surface, *Geophys. J. Int.* **83,** 31–45.

Buijze, L, L. van Bijsterveldt, H. Cremer, B. Paap, H. Veldkamp, B. B. T. Wassing, J.-D. van Wees, G. C. N. van Yperen, J. H. ter Heege, and B. Jaarsma (2019). Review of induced seismicity in geothermal systems worldwide and implications for geothermal systems in the Netherlands, *Neth. J. Geosci.* **98,** e13, doi: 10.1017/njg.2019.6.

Clarke, H., J. P. Verdon, T. Kettlety, A. F. Baird, and J.-M. Kendall (2019). Real time imaging, forecasting and management of human-induced seismicity at Preston New Road, Lancashire, England, *Seismol. Res. Lett.* **90,** 1902–1915.

Crampin, S. (1987). Geological and industrial implications of extensive-dilatancy anisotropy, *Nature* **328,** 491–496.

Deng, K., Y. Liu, and R. M. Harrington (2016). Poroelastic stress triggering of the December 2013 Crooked Lake, Alberta, induced seismicity sequence, *Geophys. Res. Lett.* **43,** 8482–8491.

Eaton, D. W. (2018). *Passive Seismic Monitoring of Induced Seismicity*, Cambridge University Press, United Kingdom.

Ellsworth, W. L. (2013). Injection-induced earthquakes, *Science* **341,** no. 1225942-1, 7.

Eyre, T. S., D. W. Eaton, D. I. Garagash, M. Zecevic, M. Venieri, R. Weir, and D. C. Lawton (2019). The role of aseismic slip in hydraulic fracturing-induced seismicity, *Sci. Adv.* **5,** eaav7172.

Eyre, T. S., D. W. Eaton, M. Zecevic, D. D'Amico, and D. Kolos (2019). Microseismicity reveals fault activation before M_W 4.1 hydraulic-fracturing induced earthquake, *Geophys. J. Int.* **218,** 534–546.

Eyre, T. S., M. Zecevic, R. O. Salvage, and D. W. Eaton (2020). A long-lived swarm of hydraulic fracturing-induced seismicity provides evidence for aseismic slip, *Bull. Seismol. Soc. Am.* **110,** 2205–2215.

Freed, A. M. (2005). Earthquake triggering by static, dynamic, and postseismic stress transfer, *Annu. Rev. Earth Planet. Sci.* **33,** 335–367.

Gajek, W., M. Malinowski, and J. P. Verdon (2018). Results of downhole microseismic monitoring at a pilot hydraulic fracturing site in Poland - Part 2: S-wave splitting analysis, *Interpretation* **6,** SH49–SH58.

Igonin, N., J. P. Verdon, J.-M. Kendall, and D. W. Eaton (2021). Large-scale fracture systems are permeable pathways for fault activation during hydraulic fracturing, *J. Geophys. Res.* **126,** e2020JB020311, doi: 10.1029/2020JB020311.

Kanamori, H., and E. E. Brodsky (2004). The physics of earthquakes, *Rep. Prog. Phys.* **67,** 1429–1496.

Kao, H., R. Visser, B. Smith, and S. Venables (2018). Performance assessment of the induced seismicity traffic light protocol for northeastern British Columbia and western Alberta, *The Leading Edge* **37,** 117–126.

Kettlety, T., J. P. Verdon, M. J. Werner, and J.-M. Kendall (2020). Stress transfer from opening hydraulic fractures controls the distribution of induced seismicity, *J. Geophys. Res.* **125,** e2019JB018794, doi: 10.1029/2019JB018794.

Kettlety, T., J. P. Verdon, M. J. Werner, J.-M. Kendall, and J. Budge (2019). Investigating the role of elastostatic stress transfer during

hydraulic fracturing-induced fault activation, *Geophys. J. Int.* **217,** 1200–1216.

Kilb, D., J. Gomberg, and P. Bodin (2002). Aftershock triggering by complete Coulomb stress changes, *J. Geophys. Res.* **107,** 2060.

Li, T., Y. Gu, Z. Wang, R. Wang, R. Chen, T. Song, and R. Wang (2019). Spatiotemporal variations in crustal seismic anisotropy surrounding induced earthquakes near Fox Creek, Alberta, *Geophys. Res. Lett.* **46,** 5180–5189.

Maxwell, S., and M. Norton (2012). Enhancing shale gas reservoir characterization using hydraulic fracture microseismic data, *First Break* **30,** 95–101.

Okada, Y. (1992). Internal deformation due to shear and tensile faults in a half-space, *Bull. Seismol. Soc. Am.* **82,** 1018–1040.

Peña-Castro, A. F., M. P. Roth, A. Verdecchia, J. Onwuemeka, Y. Liu, R. M. Harrington, Y. Zhang, and H. Kao (2020). Stress chatter via fluid flow and fault slip in a hydraulic fracturing induced earthquake sequence in the Montney formation, British Columbia, *Geophys. Res. Lett.* **47,** e2020GL087254, doi: 10.1029/2020GL087254.

Riazi, N., and D. W. Eaton (2020). Anatomy of a buried thrust belt activated during hydraulic fracturing, *Tectonophysics* **795,** 228,640.

Ruiz-Barajas, S., N. Sharma, V. Convertito, A. Zollo, and B. Benito (2017). Temporal evolution of a seismic sequence induced by a gas injection in the Eastern coast of Spain, *Nat. Sci. Rep.* **7,** 2901.

Schultz, R., R. J. Skoumal, M. R. Brudzinski, D. Eaton, B. Baptie, and W. Ellsworth (2020). Hydraulic fracturing-induced seismicity, *Rev. Geophys.* **58,** no. 3, e2019RG000695, doi: 10.1029/2019RG000695.

Schultz, R., R. Wang, Y. J. Gu, K. Haug, and G. Atkinson (2017). A seismological overview of the induced earthquakes in the Duvernay play near Fox Creek, Alberta, *J. Geophys. Res.* **122,** 492–505.

Shapiro, S. A., C. Dinske, and E. Rothert (2006). Hydraulic-fracturing controlled dynamics of microseismic clouds, *Geophys. Res. Lett.* **33,** 1–5.

Steacy, S., D. Marsan, S. S. Nalbant, and J. McCloskey (2004). Sensitivity of static stress calculations to the earthquake slip distribution, *J. Geophys. Res.* **109,** no. B04303, doi: 10.1029/2002JB002365.

Stein, R. S. (1999). The role of stress transfer in earthquake occurrence, *Nature* **402,** 605–609.

Stork, A. L., J. P. Verdon, and J.-M. Kendall (2015). The microseismic response at the In Salah Carbon Capture and Storage (CCS) site, *Int. J. Greenhouse Gas Control* **32,** 159–171.

Teanby, N. A., J.-M. Kendall, and M. van der Baan (2004). Automation of shear-wave splitting measurements using cluster analysis, *Bull. Seismol. Soc. Am.* **94,** 453–463.

Verdon, J. P., and J. J. Bommer (2021). Green, yellow, red, or out of the blue? An assessment of Traffic Light Schemes to mitigate the impact of hydraulic fracturing-induced seismicity, *J. Seismol.* **25,** 301–326.

Verdon, J. P., and A. Wuestefeld (2013). Measurement of the normal/tangential compliance ratio (Z_N/Z_T) during hydraulic fracture stimulation using shear wave splitting data, *Geophys. Prospect.* **61,** 461–475.

Verdon, J. P., D. A. Angus, J.-M. Kendall, and S. A. Hall (2008). The effects of microstructure and nonlinear stress on anisotropic seismic velocities, *Geophysics* **73,** D41–D51.

Verdon, J. P., J.-M. Kendall, and S. C. Maxwell (2010). A comparison of passive seismic monitoring of fracture stimulation due to water versus CO_2 injection, *Geophysics* **75,** MA1–MA7.

Verdon, J. P., J.-M. Kendall, and A. Wuestefeld (2009). Imaging fractures and sedimentary fabrics using shear wave splitting measurements made on passive seismic data, *Geophys. J. Int.* **179,** 1245–1254.

Wang, R., Y. J. Gu, R. Schultz, A. Kim, and G. Atkinson (2016). Source analysis of a potential hydraulic fracturing induced earthquake near Fox Creek, Alberta, *Geophys. Res. Lett.* **43,** 564–573.

Wang, R., Y. J. Gu, R. Schultz, M. Zhang, and A. Kim (2017). Source characteristics and geological implications of the January 2016 induced earthquake swarm near Crooked Lake, Alberta, *Geophys. J. Int.* **210,** no. 2, 979–988.

Wang, R., F. Lorenzo Martin, and F. Roth (2006). PSGRN/PSCMP—A new code for calculating co- and post-seismic deformation, geoid and gravity changes based on the viscoelastic-gravitational dislocation theory, *Comput. Geosci.* **32,** 527–541.

Wuestefeld, A., J. P. Verdon, J.-M. Kendall, J. Rutledge, H. Clarke, and J. Wookey (2011). Inferring rock fracture evolution during reservoir stimulation from seismic anisotropy, *Geophysics* **76,** WC159–WC168.

Zatsepin, S., and S. Crampin (1997). Modelling the compliance of crustal rock - I. Response of shear-wave splitting to differential stress, *Geophys. J. Int.* **129,** 477–494.